PCCP

Accepted Manuscript

ROYAL SOCIETY OF CHEMISTRY

www.rsc.org/pccp

Physical Chemistry Chemical Physics
CREATED USING THE RSC LaTeX PCCP ARTICLE TEMPLATE – SEE www.rsc.org/electronicfiles FOR DETAILS
ARTICLE TYPE www. rsc.org/xxxxxx | XXXXXXXX

The Role of Charge Transfer in the Oxidation State Change of Ce Atoms in the $TM_{13}/CeO_2(111)$ systems (TM = Pd, Ag, Pt, Au): A DFT+U Investigation†

Polina Tereshchuk,[a] Rafael L. H. Freire,[b] Crina G. Ungureanu,[a] Yohanna Seminovski,[a] Adam Kiejna,[c] and Juarez L. F. Da Silva*[a]

Received Xth XXXXXXXXXX 2013, Accepted Xth XXXXXXXXX 2013
First published on the web Xth XXXXXXXXXX 200X
DOI: 10.1039/b000000x

Despite extensive studies of transition metal (TM) clusters supported on ceria (CeO_2), fundamental issue as the role of the TM atoms in the change of the oxidation state of Ce atoms is still not well understood. In this work, we report a theoretical investigation based on static and *ab-initio* molecular dynamics density functional theory calculations of the interaction of 13-atom TM clusters (TM = Pd, Ag, Pt, Au) with the unreduced $CeO_2(111)$ surface represented by a large surface unit cell and employing Hubbard corrections for the strong on-site Coulomb correlation in the Ce f-electrons. We found that the TM_{13} clusters form pyramidal-like structures on $CeO_2(111)$ in the lowest energy configurations with the following stacking sequence, $TM/TM_4/TM_8/CeO_2(111)$, while TM_{13} adopts two-dimensional structures at high energy structures. TM_{13} induces a change in the oxidation state of few Ce atoms (3 of 16) located in the topmost Ce layer from Ce^{IV} (itinerant Ce f-states) to Ce^{III} (localized Ce f-states). There is a charge flow from the TM atoms to the $CeO_2(111)$ surface, which can be explained by the electronegativity difference between the TM (Pd, Ag, Pt, Au) and O atoms, however, the charge is not uniformly distributed on the topmost O layer due to the pressure induced by the TM_{13} clusters on the underlying O ions, which yields a decreasing in the ionic charge of the O ions located below the cluster and an increasing in the remaining O ions. Due to the charge flow mainly from the TM_8-layer to the topmost O-layer, the charge cannot flow from the Ce^{IV} atoms to the O atoms with the same magnitude as in the clean $CeO_2(111)$ surface. Consequently, the effective cationic charge decreases mainly for the Ce atoms that have a bond with the O atoms not located below the cluster, and hence, those Ce atoms change their oxidation state from IV to III. This increases the size of the Ce^{III} compared with the Ce^{IV} cations, which builds-in a strain within the topmost Ce layer, and hence, it contributes also to affect the location of the Ce^{III} cations and the structure of the TM_{13} clusters.

1 Introduction

Transition-metal (TM) nanoparticles (NP) supported on ceria (CeO_2) have been considered as important catalysts for a wide range of applications. For example, they promote or facilitate water-gas shift reaction for hydrogen production ($CO + H_2O \longrightarrow H_2 + CO_2$),[1–4] provide control gaseous exhaust automobile emissions (unburned or partially burned hydrocarbons, CO, NO_x),[5–8] etc. The combination of ceria with TM NP gives rise to unique synergic properties, namely, ceria support stabilizes NP against dispersion, controls the activity of NP, stores and releases oxygen and enhances rates for a number of important reactions due to the interactions with supported metals.[5,9] Thus, a wide range of studies employing the combination of experimental and theoretical techniques, or addressed independently by both approaches, have been reported for TM/CeO_2 with the aim to understand the role of the $TM–CeO_2$ interactions in the figures of merits of TM/CeO_2, e.g., Cu,[3,10–13] Rh,[2,13–15] Pd,[2,13,14,16–19] Ag,[11–13,20,21] Pt,[1,2,5,13,14,22–24] and Au,[1,3,11–13,25–29] however, our understanding is still far from being complete, as we show below.

CeO_2 crystallizes in the fluorite structure,[30] where all the Ce atoms are eightfold coordinated with an oxidation state IV. The occupied and unoccupied Ce f-states are delocalized in CeO_2,[31] while Ce atoms have oxida-

[a] *São Carlos Institute of Chemistry, University of São Paulo, PO Box 780, 13560-970, São Carlos, SP, Brazil*
[b] *São Carlos Institute of Physics, University of São Paulo, PO Box 369, 13560-970, São Carlos, SP, Brazil*
[c] *Institute of Experimental Physics, University of Wrocław, plac M. Borna 9, PL-50-204 Wrocław, Poland*

tion state III and localized *f*-states in bulk Ce_2O_3.[31,32] The formation of the most stable CeO_2 surface, namely, the unreduced oxygen-terminated $CeO_2(111)$,[16,22,33] does not change the oxidation state or the itinerant nature of the *f*-states. However, the creation of an O vacancy induces an oxidation state change from Ce^{IV} to Ce^{III}, which has been explained by the localization on the Ce atoms of the two electrons left over by the formation of the O vacancy.[34–36] The Ce^{III} cations are distributed in the vicinity of the O vacancy, where they minimize the strain build-in by the increasing of the atomic size of Ce^{III} cations (1.14 Å) compared with Ce^{IV} (0.97 Å).[37] It has been assumed that the change in the oxidation state determines the energy magnitude for O vacancy formation, which is a key parameter to understand the oxygen storage capacity.[38–40]

Thus, the adsorption of TM particles (atoms, clusters, NP) on reduced or unreduced $CeO_2(111)$ surface only contributes to increase the complexity of the effects that take place at the TM/CeO_2 catalysts. Gold adsorption studies on $CeO_2(111)$ revealed that surface O vacancies and defects play a crucial role as deep traps for Au atoms,[29] while Au particles, that are deposited on $CeO_2(111)$ films, preferentially nucleate at the step edges.[25] Furthermore, the growth of three-dimensional (3D) Ag particles on $CeO_2(111)$ films is characterized by a high sticking probability coefficient at room temperatures.[11,20,20,21,41] In addition, several studies have suggested that the adsorption of TM particles on unreduced or reduced $CeO_2(111)$ surfaces can result in oxidation state change of few Ce atoms from Ce^{IV} to Ce^{III},[42–45] which have been explained by charge transfer from the TM particles to the ceria surface,[23,27] which is expected based on the electronegativity concept,[46] however, no clear picture has been reported yet.

The electronic structure characterization of ceria and ceria-supported TM particles is a challenge for density functional theory (DFT) calculations,[31] as local or semilocal (gradient corrected) exchange-correlation (XC) functionals are not capable to take into account the localized nature of the Ce *f*-states. Plain DFT yields a metallic solution for bulk Ce_2O_3 and reduced $CeO_2(111)$ surface.[31] Therefore, DFT corrected for on-site Coulomb interactions with a Hubbard *U* parameter, DFT+*U*,[11–16,18,22,26,28,31,32,47,48] or including the nonlocal hybrid XC functional,[29,31,35,48] has to be applied. Several DFT investigations have been reported on the adsorption of single TM atoms on $CeO_2(111)$, e.g., Cu,[11,12,49] Rh,[14,15] Pd,[14,16,18] Ag,[11,12] Pt,[14,22,48] and Au.[11,12,26,27,47,50] Szabova *et al.* suggested that instead of the nucleation of Cu particles at the surface O vacancies, in oxidizing conditions, there is a formation of oxide-like CuO_4 motifs. Furthermore, Lu *et al.*[14] found out that Rh adatoms bind stronger to the $CeO_2(111)$ surface than Pd and Pt adatoms, which was recently explained by Piotrowski *et al.*[13] based on the nature of the Rh−O binding. In addition to that, it was found that Rh atoms have a preference to occupy Ce vacancy sites instead of O vacancy sites,[15] which is expected as Rh can form strong bonds with O atoms and not with Ce atoms, as was also observed for Au.[26]

The study of TM clusters supported on the reduced or unreduced $CeO_2(111)$ surface have been restricted mainly to small TM_n clusters, namely, Cu_4,[13] $Cu_{monolayer}$,[49] Ru_4,[13] Rh_4,[13,14] Pd_4,[13,14,18] Ag_4,[13] Ag_5,[21] Os_4,[13] Ir_4,[13] Pt_4,[13,14] Pt_8,[23] $Au_{1\text{-}11}$,[27] Au_3,[27,28] Au_4,[13,27] and Au_{13}.[51] From those studies, it was found that Cu_4, Pd_4, Ag_4, Pt_4, and Au_4 clusters form 3D tetrahedron structures on $CeO_2(111)$,[13,14] while Ru_4, Rh_4, Os_4, and Ir_4 clusters form two-dimensional (2D) zig-zag arrays on the $CeO_2(111)$-(2×2) substrate. It was shown that the formation of the 3D and 2D configurations depends on the strength of the TM−TM and TM−O interactions, which was discussed based on the occupation of the bonding and antibonding TM *d*-states and the hybridization with the O *p*-states. An increase in the size of the TM_n clusters, namely for Pt_n and Au_n, increases the size of the 3D conformations, which is expected. Zhang *et al.*[27] found that the Au atoms (Au_{11}-layer) in direct contact with the topmost O atoms are positively charged, which can be explained by the charge transfer concept. As mentioned above, TM particles supported on $CeO_2(111)$ indicate change in the oxidation state of few Ce atoms from Ce^{IV} to Ce^{III}, which has been attributed to the charge transfer from TM atoms to the ceria surface,[13,17,21,52] however, no clear mechanism for that has been presented.

Most of the theoretical studies reported for $TM_n/CeO_2(111)$ focused on single TM adatoms or small clusters composed by few atoms. For example, to our knowledge, only two of those studies have considered clusters of more than 10 TM atoms on ceria surfaces. Moreover, despite the suggestion about the main role of charge transfer between the TM and ceria surface played in the change of Ce oxidation state, there is no report that accounts for an atomistic mechanism for that. To improve our understanding of the interaction of TM clusters with the $CeO_2(111)$ surface, in this study, we report a theoretical investigation of 13-atom TM clusters[53,54] (TM = Pd, Ag, Pt, Au) supported on the unreduced $CeO_2(111)$ surface based on DFT+*U* calculations employing a large (4×4) $CeO_2(111)$ surface unit cell. In addition, in our work, we explain the mechanism of the charge transfer in the Ce oxidation states due to the adsorption of these

larger TM clusters on CeO_2(111) based on Bader charge concept.

2 Theoretical approach and computational details

2.1 Total energy calculations

Our total energy calculations are based on spin-polarized DFT[55,56] within the Perdew-Burke-Ernzerhof[57] (PBE) formulation of the generalized gradient approximation (GGA) as implemented in the Vienna *ab-initio* simulation package (VASP).[58,59] In order to correctly describe the itinerant or localized behavior of the Ce f-states, it is important to account for the strong on-site Coulomb correlations.[13,31,32,35,60,61] Therefore, in this work all ceria systems were described by using DFT-PBE within a Hubbard correction term U (DFT+U). We applied the rotationally invariant approach proposed by Dudarev *et al.*[62] with an effective Hubbard parameter of 4.50 eV, which is the difference between the Coulomb, U, and exchange, J, parameters ($U_{\text{eff}} = U - J$). Among several values of the U_{eff} parameter applied previously[31,63] the U_{eff} of 4.50 eV was found to be appropriate for systems containing cerium atoms.[13,35,61] It yields results similar to those obtained from hybrid-DFT with the Heyd-Scuseria-Ernzerhof[64] (HSE) functional for the unreduced and reduced CeO_2(111) surfaces.[35] In contrast with ceria-based systems, plain DFT can yields a good description of TM clusters.[65]

The electron-ion interactions were represented by projector augmented wave (PAW) potentials[66,67] provided within VASP. The following electronic states were considered as valence, $5s^14d^9$, $6s^15d^{10}$, $6s^15d^9$, $6s^15d^{10}$, $2s^22p^4$, $4f^15s^25p^65d^16s^2$, for Pd, Ag, Pt, Au, O, and Ce, respectively. The Kohn-Sham states were expanded in the plane wave basis with a cutoff energy of 466.46 eV applied for all total energy calculations. To model the TM_{13}/CeO_2(111) systems, we employed a hexagonal 4×4 surface unit cell (a = 15.30 Å) within the repeated slab geometry with six atomic layers separated by a vacuum region of about 16 Å. For those calculations, we employed the theoretical CeO_2 equilibrium lattice constant,[68] 5.48 Å, which is slightly overestimated (0.07 Å) compared with the experimental result (5.41 Å).[30] The TM_{13} clusters were adsorbed only on one side of the slab. The positions of all atoms, except for the bottom layer atoms (oxygen), were optimized. The gas-phase TM_{13} clusters were simulated using a cubic box of 20 Å size length.

For the total energy calculations, the Brillouin zone integrations for the TM_{13} and TM_{13}/CeO_2(111) systems, were performed using only the Γ-point due to the large size of the unit cells, however, a (2×2×1) Monkhorst-Pack (MP) k-point grid was used for the density of states calculations. The total energy calculations for the bulk CeO_2 structure (cubic fluorite phase) were performed using a 10×10×10 MP k-point grid. For TM_{13} clusters and bulk CeO_2 calculations, we employed a Gaussian smearing parameter, σ, of 0.01 eV, whereas for TM_{13}/CeO_2(111), it was increased to 0.10 eV to improve the electronic convergence of the calculations. For all calculations, we optimized the atomic forces until the forces on each atom were smaller than 0.025 eV/Å, with a total energy convergence of 1.0×10^{-5} eV. To obtain a better understanding of the charge transfer among the chemical species, we calculated the Bader charge[69] on every atom, which required a high density Fast Fourier Transform (FFT) grid in VASP (three times larger).

2.2 Atomic structure generation

To identify a set of reliable model structures (lowest energy configurations) for the TM_{13}/CeO_2(111) systems (TM = Pd, Ag, Pt, Au), we carried out the following procedure. We selected 13-atom clusters as this particular size has high stability among several TM systems.[53,54,70] (I) First, we obtained a reliable set of atomic configurations for the TM_{13} clusters from our previous DFT-PBE studies (about 60 configurations for each system),[53,71] which were obtained using *ab-initio* knowledge based on structural principles and are discussed elsewhere.[53] All those configurations were reoptimized using a cutoff energy of 466.46 eV. (II) For TM_{13}/CeO_2(111), *ab-initio* molecular dynamics (MD) simulation was performed, using an energy cutoff of 300 eV for about 30 ps, for an initial temperature of 2000 K, which was decreased gradually down to about 0 K. For that, we considered packed and planar TM_{13} configurations supported on CeO_2(111). For that, only the clusters and the two topmost surface layers were allowed to relax along the simulation. (III) We selected about 18 atomic configurations equally spaced along the MD simulation, which were optimized using the conjugated gradient algorithm as implemented in VASP. (IV) The obtained lowest energy configurations of TM_{13}/CeO_2(111) were subsequently used for crossover calculations among the different TM_{13}/CeO_2 systems.

3 Results

3.1 Gas phase TM_{13} clusters

The putative lowest energy structure and a selected high energy isomer for the TM_{13} clusters are shown in Fig-

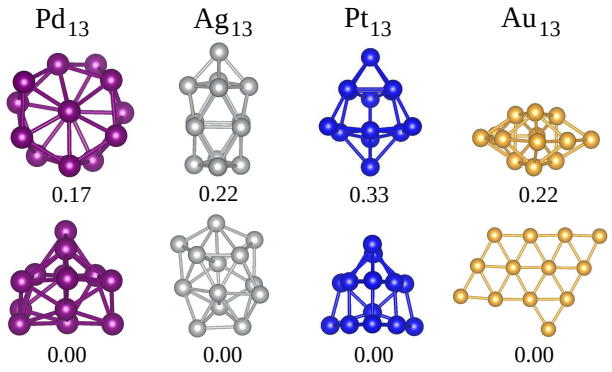

Fig. 1 The lowest energy (lower row) and selected high energy (upper row) configurations of the TM_{13} clusters in gas-phase. The relative total energy per cluster (in eV) are indicated.

ure 1. The relative total energies ($\Delta E_{tot} = E_{tot}^{Config\text{-}i} - E_{tot}^{lowest}$), effective coordination number (ECN) in number of nearest neighbors (NNN),[72–74] average weighted bond length (d_{av}), binding energy per atom (E_b), and total magnetic moment (m_T) are summarized in Table 1. Furthermore, the ΔE_{tot} results for all configurations are reported in the supporting information. As discussed previously,[53] instead of the compact 13-atom icosahedron (ICO) structure with ECN = 6.46, the Pd_{13}, Ag_{13}, Pt_{13}, and Au_{13} clusters adopt structures with ECN from 3.78 (Au_{13}) to 5.66 (Ag_{13}), which are −0.27, −1.26, −3.43, and −1.78 eV/cluster lower in energy than ICO, respectively. As expected from the occupation of the bonding and antibonding states in the TM_{13} clusters,[53] we obtained shorter bond lengths for Pd_{13} and Pt_{13} due to the partial occupation of the *d*-states, while they are larger for Ag_{13} and Au_{13} due to the occupation of the antibonding *d*-states, and hence, the binding energy follows the same trend, Table 1. For Au_{13}, the ground state is a 2D structure, however, its first high energy isomer is a 3D structure, which becomes the ground state structure upon the addition of spin-orbit coupling for the valence states.[53] We found that magnetic moments for all the lowest energy clusters are larger for Pd_{13} (m_T = 8 μ_B) due to the stronger localization of the 4*d*-states compared with the 5*d*-states of Pt and Au.

Table 1 Structural, energetic, and magnetic properties of the TM_{13} clusters. Relative total energy per cluster (ΔE_{tot}), effective coordination number (ECN) in number of nearest neighbors (NNN), average weighted bond lengths (d_{av}), binding energy per atom (E_b), and total magnetic moment (m_T).

TM_{13}	ΔE_{tot} (eV)	ECN (NNN)	d_{av} (Å)	E_b (eV)	m_T (μ_B)
Pd	0.17	5.37	2.67	−2.20	6
	0.00	5.65	2.67	−2.37	8
Ag	0.22	5.05	2.81	−1.45	1
	0.00	5.66	2.83	−1.67	1
Pt	0.33	4.36	2.59	−3.46	0
	0.00	4.28	2.58	−3.79	2
Au	0.22	4.97	2.78	−1.91	1
	0.00	3.78	2.68	−2.13	1

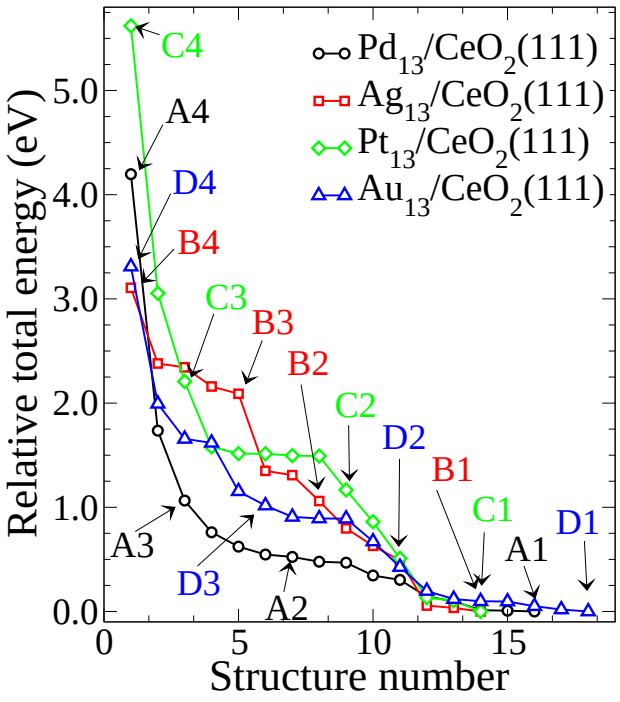

Fig. 2 Relative total energies with respect to the lowest energy structure for all model $TM_{13}/CeO_2(111)$ structures considered in this work. The structures indicated by label are shown in Figure 3.

3.2 $TM_{13}/CeO_2(111)$

To improve our understanding of the interaction of TM_{13} clusters with $CeO_2(111)$, we performed several analyses. The results are shown in Figures 2 (relative energy trends), 3 (lowest energy configurations), and 4 (density of states), Tables 2 (geometric parameters) and 3 (Bader charges). In agreement with previous DFT+*U* calculations,[13,35,44,75] we found that all the Ce atoms are in the oxidation state IV in the unreduced $CeO_2(111)$ surface, the Ce *f*-states show an itinerant behavior, and small interlayer relaxations are observed for the topmost surface layer (Δd_{O-Ce} = 1.39 %) due to the strong stability of the CeO_2 lattice (Coulomb interactions among the ions).

3.2.1 Relative total energies Despite the geometric similarity among the model structures calculated for the Pd_{13}, Ag_{13}, Pt_{13}, and Au_{13} clusters supported on $CeO_2(111)$, we found that the relative total energy spans over the energy window of 4.20, 3.11, 5.62, and 3.31 eV, respectively, Figure 2, which corresponds to the energy difference between 3D and 2D structures. The smallest energy range occurs for the TM_{13} systems with a complete occupation of the bonding and antibonding *d*-states (Ag, Au), which is consistent with previous results for gas-phase and supported TM clusters.[13,53]

3.2.2 Atomic structures In the lowest energy configuration (A1, B1, C1, D1), the TM_{13} clusters form 3D pyramidal-like compact structures on $CeO_2(111)$, in which eight TM atoms are in direct interaction with the oxygen terminated $CeO_2(111)$ surface. The TM_8 atoms form a hexagonal-like base, which can be attributed to the hexagonal symmetry of the surface layers and to the tendency of the TM atoms to form compact structures. Four TM atoms are located on the hollow sites on the 8-atoms layer, and the last TM atom is located on the hollow site formed by the second 4-atom layer, which can be seen in Figure 3. That is, we obtained the following stacking, $TM/TM_4/TM_8/CeO_2(111)$, for all studied systems. We would like to stress that this particular configuration was not provided as input, i.e., the pyramidal-like structures are formed from high-temperature MD simulation starting even from a 2D configuration.

In the highest energy configurations (A4, B4, C4, D4), all the 13-atom clusters form 2D structures on $CeO_2(111)$, which are 4.20, 3.11, 5.62, and 3.31 eV higher in energy than the 3D pyramidal-like structure for Pd_{13}, Ag_{13}, Pt_{13}, and Au_{13}, respectively. Thus, at first sight, we would conclude that the Pd_{13} and Pt_{13} clusters have a stronger preference for 3D structures, however, this is in contrast with our analysis taken into account the magnitude of the binding energy among the TM atoms. For example, the ratio between the relative total energy (ΔE_{tot}) and cluster binding energy (E_b) is nearly the same for Pd_{13} and Ag_{13} (i.e., 1.77 and 1.86) and for Pt_{13} and Au_{13} (i.e., 1.48 and 1.55). Thus, it indicates a stronger preference of 3D structures for Pd_{13} and Ag_{13} supported on $CeO_2(111)$ than for Pt_{13} and Au_{13}, which is consistent with the smaller ECN results obtained for Pt_{13} and Au_{13} in gas-phase.

The pyramidal-like structure is far away from the lowest energy gas-phase TM_{13} structures, Figure 1. For example, we found a decrease in the ECN of Pd_{13} and Ag_{13} on $CeO_2(111)$ by 9.38 and 10.60 % compared with gas-phase clusters, while it increased by 17.52 and 28.31 % for Pt_{13} and Au_{13}, respectively. However, we found small changes in the average TM−TM bond lengths, which increases from 0.02 Å for Pd_{13} and Ag_{13} to 0.09-0.14 Å for Pt_{13} and Au_{13}, which indicates that the TM−TM bonds are not strongly affected by the substrate.

3.2.3 The role of the Ce oxidation states in the strain release The TM_{13}–$CeO_2(111)$ interaction induces a change in the oxidation state of few Ce atoms located in the topmost Ce layer from Ce^{IV} to Ce^{III}, which is in agreement with previous results,[11–13,15,17,21,23,25,52] and can be identified by the local magnetic moments and localization of the Ce *f*-states (density of states). For example, Ce^{IV} has a zero local magnetic moment, while it increases up to 1 μ_B for Ce^{III} cations due to the Ce *f*-localization. The differences in the localization of the *f*-states affect the electronic screening, and hence, the size of the atomic radius of the Ce cations (0.97 Å for Ce^{IV}, and 1.14 Å for Ce^{III}).[37]

For all $TM_{13}/CeO_2(111)$ configurations, the Ce^{III} are located in the topmost Ce layer (dark green atoms in Figure 3), and hence, there is a compressive strain built-in in this layer. Thus, relaxations should occur to release the strain energy, however, due to the constraint imposed by the slab (*xy*-plane), deformations can occur only within the *xy*-plane and perpendicular to the *xy*-plane. Thus, there is a decreasing in the in-plane distance between the Ce^{IV} atoms, which contributes to increase of the distance between the Ce^{IV} and Ce^{III} atoms. Furthermore, as a consequence of the Ce oxidation state change, there is an increase in the Ce−O bond lengths. For example, the Ce^{IV}−O bond lengths are smaller (2.35 Å to 2.36 Å) than those between Ce^{III}−O (2.47 Å).

3.2.4 Location of the Ce^{III} atoms Although the TM atoms play a key role in the change of the oxidation state, the Ce^{III} atoms are not located directly below the TM atoms for all configurations. For example, in the lowest energy configurations, the Ce^{III} atoms are located in the vicinity of the TM_{13} clusters, however, at high energy configurations, the Ce^{III} atoms can be located below the cluster, which is the case for the 2D configurations. The location of the Ce^{III} atoms have two origins, namely, surface distortions and the charge transfer between the TM and O atoms. Furthermore, we would like to point out that only few Ce atoms change their oxidation state, namely, 18.75 % (3 in 16 Ce atoms in the topmost surface layer). This finding differs from our previous work[13] on the $TM_4/CeO_2(111)$ systems where, depending on the TM element, the number of Ce atoms in the Ce^{III} oxidation state increases from 25 % to 50 %, for Pd_4, Pt_4 and Ag_4, Au_4 clusters, respectively, which can be explained by the smaller size of the unit cell than that applied in the present work.

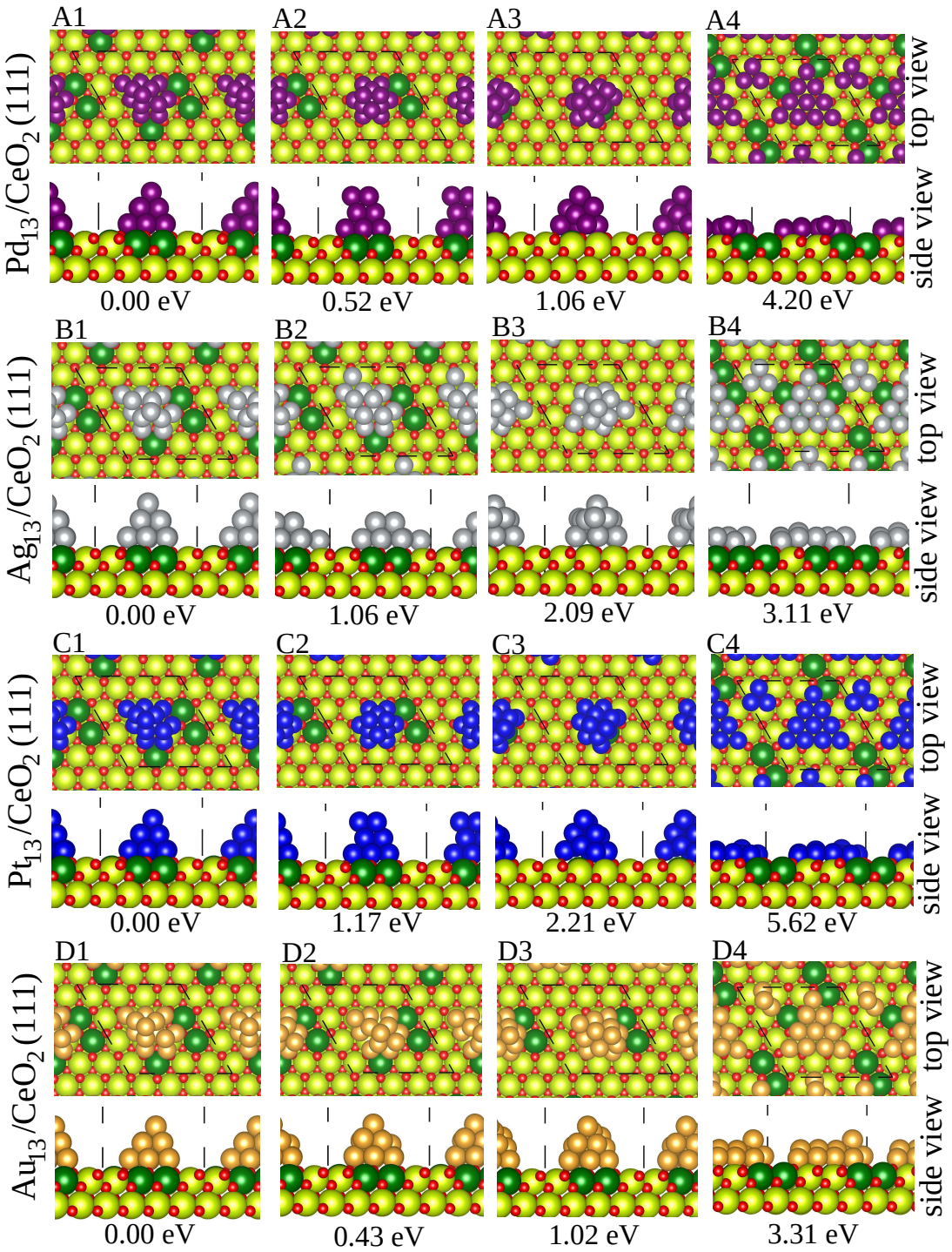

Fig. 3 Lowest energy configurations for the $TM_{13}/CeO_2(111)$ structures with their relative total energies (top and side views). The O, TM, and Ce atoms are indicated by small (red), medium (purple, Pd; gray, Ag; blue, Pt; and yellow-orange, Au), and large spheres. The Ce atoms are separated into two groups, namely, Ce^{III} (dark green) and Ce^{IV} (light green).

3.2.5 Adsorption energy To obtain a better understanding of the interaction of TM_{13} with $CeO_2(111)$, we calculated the adsorption energy, E_{ad}, using the follow-

Table 2 Structural, energetic, and magnetic properties of the lowest energy $TM_{13}/CeO_2(111)$ configurations. Effective coordination number (ECN) of pyramidal TM_{13} clusters supported on $CeO_2(111)$ in number of nearest neighbors (NNN), average weighted bond length distances (d_{TM-TM}, d_{O-TM}, $d_{Ce^{IV}-O}$, and $d_{Ce^{III}-O}$), interlayer spacing relaxations (Δd_{12} and Δd_{23}), adsorption binding energy of the TM_{13} cluster, calculated with respect to the energy of a gas-phase cluster ($E_{ad}^{cluster}$) and with respect to the TM_{13} layer (E_{ad}^{layer}), and the total magnetic moment (m_T).

TM_{13}	ECN (NNN)	d_{TM-TM} (Å)	d_{O-TM} (Å)	$d_{Ce^{IV}-O}$ (Å)	$d_{Ce^{III}-O}$ (Å)	Δd_{12} (%)	Δd_{23} (%)	$E_{ad}^{cluster}$ (eV)	E_{ad}^{layer} (eV)	m_T (μ_B)
Pd	5.12	2.69	2.07	2.36	2.47	11.89	2.30	−6.24	−10.47	5.15
Ag	5.06	2.85	2.22	2.35	2.47	11.57	2.36	−4.84	−9.11	3.00
Pt	5.03	2.67	2.05	2.35	2.47	13.36	1.96	−7.29	−13.06	4.59
Au	4.85	2.82	2.15	2.35	2.47	9.98	2.22	−4.35	−9.34	3.00

ing equation,

$$E_{ad} = E_{tot}^{TM_{13}/CeO_2(111)} - E_{tot}^{CeO_2(111)} - E_{tot}^{TM_{13}}, \quad (1)$$

where $E_{tot}^{TM_{13}/CeO_2(111)}$ is the total energy of the lowest energy $TM_{13}/CeO_2(111)$ configuration, $E_{tot}^{CeO_2(111)}$ and $E_{tot}^{TM_{13}}$ are the total energies of the lowest energy structure for the clean $CeO_2(111)$ surface and TM_{13} clusters, respectively. For the adsorption energy with respect to the gas-phase TM_{13} clusters, we computed $E_{ad}^{cluster}$, using the total energy of the TM_{13} clusters in gas-phase. However, as mentioned above, the atomic structure of the supported TM_{13} clusters is different from their respective gas-phase lowest energy structures. Therefore, to take into account only the TM_{13}–$CeO_2(111)$ interactions without effects from the structure deformations, we calculated the adsorption energy with respect to the TM_{13} layer, E_{ad}^{layer}, where $E_{tot}^{TM_{13}}$ is the total energy of 13-atom clusters calculated using the same unit cell as for clean surface and frozen atomic positions obtained from the $TM_{13}/CeO_2(111)$ system. Both adsorption energies are summarized in Table 2.

We found that the absolute value of $E_{ad}^{cluster}$ decreases with the increased occupation of the *d*-states, from Pd to Ag, and from Pt to Au, which is in agreement with previous results obtained for $TM_4/CeO_2(111)$,[13] and it can be explained by the interaction of the O *p*-states with the occupied TM antibonding states for Ag and Au, and the occupation of the antibonding *d*-states contributes to decrease the adsorption energy. In comparison to single TM atoms[76] or TM_4 clusters supported on $CeO_2(111)$,[13] the adsorption energy, $E_{ad}^{cluster}$/atom, distinctly decreases for larger cluster size, which can be explained by the number of TM atoms that bind directly to the oxygen surface, i.e., three TM atoms for $TM_4/CeO_2(111)$ (75 %), while there are only eight TM atoms for $TM_{13}/CeO_2(111)$ (62 %).

As expected from its definition, $|E_{ad}^{cluster}| < |E_{ad}^{layer}|$, however, the same trends are observed for both adsorption energies, which shows that the structure relaxations do not affect the trends. We found that the differences in the adsorption energies ($\Delta_{ad} = E_{ad}^{cluster} - E_{ad}^{layer}$) range from 4.2 to nearly 5.0 eV, which indicates large deformations in the TM_{13} and $CeO_2(111)$ systems. Using the total energies employed to calculate E_{ad}^{layer}, we found an energy gain due to the relaxation of the $CeO_2(111)$ surface upon removing the TM_{13} layers from 2.87 (Ag) to 3.81 eV (Pt), which indicates a strong perturbation of the topmost $CeO_2(111)$ layers due to the deformations of the topmost layers to release the compressive strain generated by the change in the oxidation states of the Ce atoms and the changes generated due to the interaction with the TM atoms. The energy gain upon the relaxation of the TM_{13} layers without the substrate varies from 0.75 (Ag) to 1.63 eV (Au).

3.2.6 Charge transfer (Bader analysis) To obtain a better understanding of a charge flow among the TM_{13} clusters and the $CeO_2(111)$ surface, we calculated the charge transfer between the chemical species in the lowest energy configurations using the Bader charge concept.[77,78] The average Bader charges, Q_B, for the TM_{13} clusters and topmost three layers (O^{L1}–Ce^{L2}–O^{L3}) are summarized in Table 3, while the Bader charge for every atom is reported in the supporting information. Here, we defined the effective charge in number of electrons (*e*) on every atom as $Q_{eff} = Z_v - Q_B$ ($Z_v = 6\,e$, $10\,e$, $11\,e$, $12\,e$, $10\,e$ and $11\,e$ for O, Pd, Ag, Ce, Pt, and Au, respectively), and hence, a negative or positive values for Q_{eff} indicate an anion or cation, respectively. Applying the charge neutrality condition within the cluster and topmost three layers, $\Delta Q_{eff} = \sum_i (Z_v^i - Q_B^i)$, we obtained that $\Delta Q_{eff} = 0.19\,e$, $0.22\,e$, $-0.13\,e$ and $0.15\,e$ for Pd, Ag, Pt, and Au on $CeO_2(111)$, respectively, which implies a maximum difference of about $3 \times 10^{-3}\,e$/atom. Thus, we can conclude that almost 100 % of the charge transfer from

Table 3 Average Bader charge, Q_B (in number of e), on different atoms of the $TM_{13}/CeO_2(111)$ systems. Here, TM_{top}, TM_{mid}, and TM_{bot} indicate the TM atoms in the top, middle, and bottom layer of the pyramidal TM_{13} cluster supported on $CeO_2(111)$. The TM_{bot} atoms (8-atom hexagonal layer) are separated into two groups, namely, center atom, $TM_{bot\text{-}c}$, and border atoms, $TM_{bot\text{-}b}$. The 16 Ce atoms in the topmost Ce layer are separated into two groups, namely, Ce^{III} and Ce^{IV}, while the 16 O atoms in the topmost surface layer are separated by O^{L1}_{CeTM} (for O atoms bound to Ce and TM atoms) and O^{L1}_{Ce} (for O atoms which bind only to Ce atoms), while O^{L2}_{Ce} indicates the O atoms in the second O layer.

Atom	Pd_{13}	Ag_{13}	Pt_{13}	Au_{13}
TM_{top}	10.08	11.01	10.22	11.16
TM_{mid}	10.00	10.96	10.01	11.03
$TM_{bot\text{-}b}$	9.88	10.86	9.90	10.88
$TM_{bot\text{-}c}$	9.72	10.84	9.64	10.77
Ce^{III}	9.86	9.96	9.87	9.86
Ce^{IV}	9.63	9.71	9.64	9.62
O^{L1}_{CeTM}	7.13	7.13	7.10	7.13
O^{L1}_{Ce}	7.21	7.15	7.21	7.20
O^{L2}_{Ce}	7.21	7.17	7.22	7.21

the 13-atom clusters is located within the three topmost $CeO_2(111)$ surface layers.

Due to the large difference in the electronegativity of the Ce (1.12) and O (3.44) atoms,[46] one may expect a large charge transfer between the Ce and O atoms, which is indeed supported by our results. For example, $Q^{Ce^{IV}}_{eff} = 2.40\,e$ and $Q^{O}_{eff} = -1.20\,e$ in the crystalline bulk CeO_2 phase, which are nearly the same as in the topmost layers of the clean $CeO_2(111)$ surface (i.e., $2.38\,e$ and $-1.20\,e$). This indicates only a tiny perturbation in the effective charge due to the surface and is consistent with the small interlayer $CeO_2(111)$ relaxations.

For the TM atom in the topmost layer of the pyramidal TM_{13} structure, $Q^{TM}_{eff} = -0.08\,e$ (Pd), $-0.01\,e$ (Ag), $-0.22\,e$ (Pt), and $-0.16\,e$ (Au), which shows the differences in the localization of the 4*d*- and 5*d*-states. However, the effective charge is nearly zero for the TM atoms of the second layer, namely, $Q^{TM}_{eff} = 0.00\,e$ (Pd), $0.04\,e$ (Ag), $0.01\,e$ (Pt), and $0.03\,e$ (Au), which indicates a bulk-like behavior. For the third TM layer, which is in a direct contact with the O atoms, the effective charge on the TM atoms is positive due to the charge transfer from the TM atoms to the $CeO_2(111)$ surface. This can be explained by the electronegativity difference of the Pd (2.20), Ag (1.93), Pt (2.28), Au (2.54) and O (3.44) atoms. We found an effective charge transfer from the Pd_{13}, Ag_{13}, Pt_{13}, and Au_{13} clusters to the $CeO_2(111)$ surface of $1.04\,e$, $1.29\,e$, $0.80\,e$, and $0.79\,e$, respectively, which should affect the effective charge on the O and Ce atoms.

The Bader charge of the O atoms that bind directly to the TM and Ce atoms (8 atoms), O^{L1}_{CeTM}, is decreased compared with the clean $CeO_2(111)$ surface, while that of the remaining eight O atoms is increased slightly (i.e., nearly $0.01\,e$ to $0.03\,e$ per O atom). This can be explained by the pressure exerted by the TM_{13} cluster on the surface. Thus, we found that in comparison with the clean $CeO_2(111)$ surface, the topmost O layer also looses charge, on the average, $0.47\,e$, $0.95\,e$, $0.71\,e$ and $0.55\,e$ for the Pd/Ce, Ag/Ce, Pt/Ce, and Au/Ce systems, respectively. The effective charge in the Ce layer increases, respectively by $0.92\,e$, $2.26\,e$, $1.08\,e$ and $0.79\,e$ compared with the clean surface, while the changes in the second O layer depend on the TM cluster. For example, the second O layer gains $0.17\,e$, $0.33\,e$ and $0.17\,e$ for Pd, Pt, and Au clusters while it decreases the charge by $0.47\,e$ for $Ag_{13}/CeO_2(111)$.

The above trends can be explained as follows. Due to the electronegativity differences between the Pd, Ag, Pt, Au and O atoms, there is a charge transfer from the TM clusters to the $CeO_2(111)$ surface, which will be accumulated in the O layers. The pressure induced by the cluster decreases the charge on the O atoms below the cluster and increases it for the remaining O atoms, however, there is a net decrease in the total electronic charge. Thus, due to the charge transfer from the TM to the O atoms and the pressure induced by the TM cluster, the charge cannot flow from the Ce^{IV} atoms to the O atoms as in the case of a clean $CeO_2(111)$ surface, where the cationic and anionic charges on the Ce and O atoms are $2.38\,e$ and $-1.20\,e$, respectively. Thus, the effective cationic Bader charge decreases for all Ce atoms, in particular, it decreases substantially (nearly by $0.25\,e$ per Ce atom) for few Ce atoms that have a bond with the O atoms not located below the cluster (O atoms with the largest ionic charges).

A small change in the effective charge (i.e., $\sim 0.05\,e$) of the Ce^{IV} atoms is not enough to induce a change in the nature of the Ce *f*-states, however, an effective change of $0.25\,e$ affects the behavior of the Ce *f*-states, namely, from itinerant (Ce^{IV}) to localized (Ce^{III}). For the four TM systems, the number of Ce^{III} atoms is the same in the lowest energy configurations, however, there are small differences in the magnitude of the charge transfer from TM clusters to the surface, which indicates that the strain build-in by the large size of the Ce^{III} atoms compared with Ce^{IV} might play a crucial role.

3.2.7 Electronic structure To obtain a better understanding of the electronic properties, we calculated the

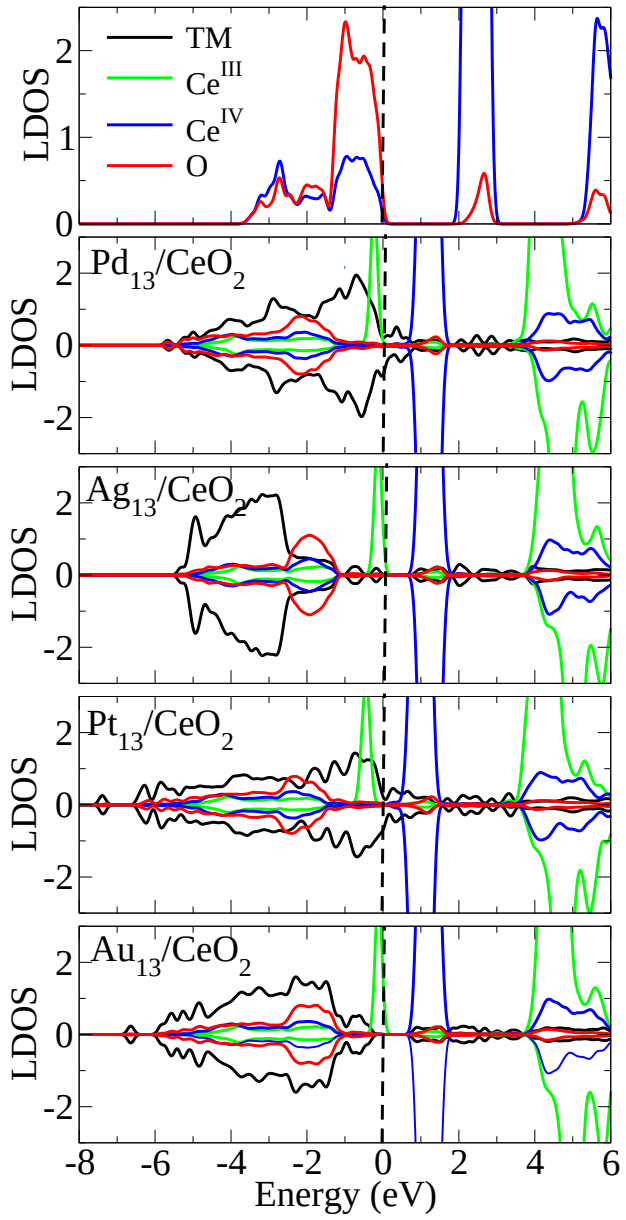

Fig. 4 Atom resolved local density of states (LDOS) for the $TM_{13}/CeO_2(111)$ systems in the lowest energy configuration for each system. For comparison the uppermost panel shows the LDOS of the clean $CeO_2(111)$ surface. The vertical dashed line (black) indicate the Fermi level.

atom resolved local density of states (LDOS), which was averaged for the TM, O, Ce^{III}, and Ce^{IV} atoms located in the TM_{13} clusters and two topmost surface layers. The results are shown in Figure 4. As expected, for the clean $CeO_2(111)$ surface, in the energy range from −8.0 eV to the Fermi level (zero energy), the valence band is dominated by O *p*-states derived from the O 2*p* and Ce^{IV} *d*-states (bottom of the valence band, derived from Ce 5*d*-states) and itinerant Ce *f*-states (top of the valence band, derived from Ce 4*f*-states). The center of gravity of the peak of the remaining unoccupied Ce states is located at about 2.5 eV above the Fermi level, with a bandwidth of about 1.0 eV, and an energy separation of about 2.0 eV between the occupied and unoccupied Ce *f*-states.

As mentioned above, the adsorption of the TM_{13} clusters changes the oxidation state of few Ce atoms on $CeO_2(111)$ from IV (itinerant) to III (localized), which implies a narrow bandwidth for the localized Ce *f*-states (located near to the Fermi energy), while the itinerant Ce *f*-states have a wide bandwidth as in the clean $CeO_2(111)$ surface and start at about 1.0 eV to 2.0 eV below the localized states. Thus, it results that the localization of the Ce *f*-states creates an energy gap in the valence band between the localized and the itinerant Ce states. Furthermore, the O *p*-states near to the Fermi level is almost negligible, and hence, we expect a small (large) hybridization between the O *p*-states and the localized (itinerant) Ce *f*-states. The unoccupied *f*-states derived from the Ce^{IV} atoms are located 1.0 eV above the Fermi energy, while the unoccupied *f*-states derived from the Ce^{III} start at about 4.0 eV above the Fermi level. That is, compared with the Ce^{IV} cations, the localization of one of the Ce *f*-states, which is occupied by nearly one electron, increases the split between the occupied and unoccupied *f*-states associated with that particular Ce^{III} cation. We would like to mention that the exact position of the unoccupied Ce *f*-states derived from Ce^{III} ions depend on the magnitude of the effective Hubbard *U* parameter, namely, U_{eff}.

As expected, the DOS associated with the TM atoms is dominated by the TM *d*-states, and the main difference is only at the Fermi level. The Pd/Ce and Pt/Ce systems have a small DOS contribution at the Fermi level, which decreases to zero for the Ag/Ce and Au/Ce systems. However, the Au *d*-states spread over a wider range compared with Ag *d*-states. Furthermore, one can notice that the Pd and Pt *d*-states spread over a wider energy range than the Ag and Au *d*-states with a tail above the Fermi level, which can explain the stronger binding of the Pd and Pt atoms to the surface and large charge transfer between Pd, Pt and O atoms.

To obtain further insights from the electronic $TM_{13}/CeO_2(111)$ states, we calculated the center of gravity of the occupied TM *d*-states with respect to the Fermi level, ϵ_d, which correlates with the magnitude of the adsorption energy of small chemical species on the TM sys-

Table 4 Center of gravity of the occupied *d*-states for the gas-phase TM_{13} clusters, frozen TM_{13} clusters (without CeO_2(111) substrate), TM_{13} clusters supported on CeO_2(111), compact TM(111) surface, and the bulk TM. ϵ_d^{av} indicates the average of the *d*-band center, while L1, L2, and L3 indicates the first layer, second, and third layers in the pyramid-like TM_{13} structures supported on CeO_2(111), and first and second layers in the TM(111) surfaces. All results are given in eV.

	ϵ_d^{av}	ϵ_d^{L1}	ϵ_d^{L2}	ϵ_d^{L3}
Bulk Pd fcc	−2.20			
Pd(111)		−1.86	−2.26	
Gas-phase Pd_{13}	−1.75			
Pd_{13}/CeO_2(111)	−1.96	−1.25	−1.90	−2.09
Frozen Pd_{13}	−1.61	−1.41	−1.84	−1.53
Bulk Ag fcc	−4.19			
Ag(111)		−4.00	−4.23	
Gas-phase Ag_{13}	−3.90			
Ag_{13}/CeO_2(111)	−3.84	−3.70	−3.89	−3.84
Frozen Ag_{13}	−4.07	−4.35	−4.22	−3.96
Bulk Pt fcc	−3.02			
Pt(111)		−2.47	−3.01	
Gas-phase Pt_{13}	−2.49			
Pt_{13}/CeO_2(111)	−2.52	−1.66	−2.43	−2.68
Frozen Pt_{13}	−2.14	−2.06	−2.41	−2.02
Bulk Au fcc	−3.76			
Au(111)		−3.31	−3.67	
Gas-Phase Au_{13}	−2.36			
Au_{13}/CeO_2(111)	−3.32	−3.09	−3.30	−3.35
Frozen Au_{13}	−3.05	−3.37	−3.23	−2.91

tems.[79,80] Furthermore, for comparison, we calculated also the *d*-band center for the bulk, gas-phase TM_{13} clusters, frozen TM_{13} clusters (without CeO_2(111) substrate) and the TM(111) surfaces. For TM(111), we employed our previous surface results.[81–83] All results are summarized in Table 4.

As expected, we found that a reduction in the coordination of the TM atoms shift the center of *d*-states towards the Fermi level, which can be seen for all systems compared with their respective bulk phase and compact clean surfaces. For example, the topmost TM atom in the pyramidal-like structure has the lowest coordination, and hence, we observed a strong shift towards the Fermi level, however, the magnitude of the shift depends strongly on the chemical species. For Pd and Pt, it is nearly 1.0 eV, while is about 0.30 eV for Ag and Au. Furthermore, the center of gravity for the TM_8 layer, which is in contact with the CeO_2(111) surface, are nearly to the values observed for the compact surfaces. Thus, although the TM atoms are in direct contact with the O topmost surface layer and charge transfer take place from TM_8 to the surface, the effect on the *d*-states is not strong as the reduction in the coordination. From the present results, we can conclude that a wide range of values for the center of gravity can be observed for large TM particles supported on CeO_2(111), which can play a crucial role in chemical reactions.

4 Summary

In this work, we reported a DFT+*U* investigation of the interaction of 13-atom clusters (Pd_{13}, Ag_{13}, Pt_{13}, Au_{13}) with the unreduced CeO_2(111) surface employing a (4×4) surface unit cell, which is important to account for the strain built-in in the topmost surface layers. Our model structures were based on *ab-initio* MD simulations starting from 2D to 3D 13-atom configurations supported on the CeO_2(111) surface. In the lowest energy configurations, we found that the TM_{13} clusters form pyramid-like structures on CeO_2(111) with the following stacking sequence, $TM/TM_4/TM_8/CeO_2$(111), i.e., eigth TM atoms interact directly with the O-terminated CeO_2(111), four of them are located in the hollow sites formed by the 8-atom layer, and the remaining TM atom is located on top of the second layer (hollow). Thus, compared with the gas-phase TM_{13} clusters, the ECN value decreases for Pd_{13} and Ag_{13}, and increases for Pt_{13} and Au_{13}, as Pt_n and Au_n clusters have a strong preference for nearly 2D configurations in gas-phase. The high energy configurations form 2D layered structures, which indicates that those structures can be observed only at very high temperatures.

As expected from previous studies, we found that the adsorption of TM_{13} clusters on CeO_2(111) changes the oxidation state of few Ce atoms (3 of 16) from Ce^{IV} (Ce *f*-states are itinerant) to Ce^{III} (Ce *f*-states are localized), which are located in the topmost Ce layer. The differences in the localization of the *f*-states affect the electronic screening, and hence, the size of the atomic radius of the Ce cations (0.97 Å for Ce^{IV} and 1.14 Å for Ce^{III}), which was verified by the Ce−O bond lengths, i.e., larger for Ce^{III}−O. Thus, there is a compressive strain built-in in the topmost Ce layer, which is released by decreasing the distance between the Ce^{IV} atoms in-plane and by increasing the distance between the Ce^{IV} and Ce^{III} atoms. In the lowest energy configurations, the Ce^{III} atoms are located in the vicinity of the TM_{13} clusters, however, at high energy configurations, the Ce^{III} atoms can be located below the cluster, which is the case for the 2D configurations.

Based on the Bader charge concept and above analy-

ses, we can explain the change in the Ce oxidation states due to the adsorption of TM_{13} clusters on $CeO_2(111)$ as follows. There is a charge flow mainly from the TM_8 layer to the surface, in particular, to the topmost O layer, which can be explained by the electronegativity difference between the Pd, Ag, Pt, Au) and O atoms, however, the charge is not uniformly distributed on the O layer due to the pressure induced by the cluster on the underlying ions and it modifies the electron density (strong TM−O bonding), which yields a decreasing in the ionic charge of the O ions below the cluster and an increasing in the remaining O ions. Due to the charge flow from the TM_8-layer to the topmost O layer, the charge cannot flow from the Ce^{IV} atoms to the O atoms located in the topmost layer with the same magnitude as in the clean $CeO_2(111)$ surface (2.38 e for Ce and −1.20 e for O). Consequently, the effective cationic charge decreases mainly for few Ce atoms (3 in 16 using a (4×4) surface unit cell) that have a bond with the O atoms not located below the cluster (nearly 0.25 e per Ce atom), and hence, those Ce atoms change their oxidation state from IV to III.

The TM atoms have an electronegativity smaller than O, and the binding of TM atoms with O atom is relatively stronger, which plays an important role in the pressure induced by the clusters on O ions located below the cluster. Thus, the present explanation is general and it can be applied to explain the interaction of TM particles with CeO_2 oxides.

5 Acknowledgments

We thank the São Paulo Science Foundation (FAPESP), the National Counsel of Technological and Scientific Development (CNPq), and the Brazilian National Program of PosDocs (PNPD/CAPES) for the financial support. We also thank the infrastructure of the Centro de Informática de São Carlos, Universidade de São Paulo, for hosting the computer cluster.

6 Supporting Information

Extra density of states and the Bader charges results for every atom summarized in the supporting information.

References

1 Q. Fu, H. Saltsburg and M. Flytzani-Stephanopoulos, *Science*, 2003, **301**, 935–938.
2 P. Panagiotopoulou and D. I. Kondarides, *Catal. Today*, 2006, **112**, 49–52.
3 J. A. Rodriguez, P. Liu, J. Hrbek, J. Evans and M. Pérez, *Angew. Chem. Int. Ed.*, 2007, **46**, 1339–1332.
4 J. B. Park, J. Graciani, J. Evans, D. Stacchiola, S. D. Senanayake, L. Barrio, P. Liu, J. F. Sanz, J. Hrbek and J. A. Rodriguez, *J. Am. Chem. Soc.*, 2010, **132**, 356–363.
5 A. F. Diwell, R. R. Rajaram, H. A. Shaw and T. J. Truex, *Stud. Surf. Sci. Catal.*, 1991, **71**, 139–152.
6 J. Kašpar, P. Fornasiero and M. Graziani, *Catal. Today*, 1999, **50**, 285–298.
7 M. Shelef and R. W. McCabe, *Catal. Today*, 2000, **62**, 35–50.
8 J. Kašpar, P. Fornasiero and N. Hickey, *Catal. Today*, 2003, **77**, 419–449.
9 M. Cargnello, V. V. T. Doan-Nguyen, T. R. Gordon, R. E. Diaz, E. A. Stach, R. J. Gorte, P. Fornasiero and C. B. Murray, *Science*, 2013, **341**, 771–773.
10 V. Matolín, L. Sedlaćěk, I. Matolínová, F. Šutara, T. Skála, B. Šmd́, J. Libra, V. Nehasil and K. C. Prince, *J. Phys. Chem. C*, 2008, **112**, 3751–3758.
11 M. M. Branda, N. C. Hernández, J. F. Sanz and F. Illas, *J. Phys. Chem. C*, 2010, **114**, 1934–1941.
12 L. Cui, Y. Tang, H. Zhang, L. G. H. Jr., C. Ouyang, S. Shi, H. Li and L. Chen, *Phys. Chem. Chem. Phys.*, 2012, **14**, 1923–1933.
13 M. J. Piotrowski, P. Tereshchuk and J. L. F. Da Silva, *J. Phys. Chem. C*, 2014, **188**, 21438–21446.
14 Z. Lu and Z. Yang, *J. Phys.: Condens. Matter*, 2010, **22**, 475003.
15 Z. Lu, Z. Yang, K. Hermansson and C. W. M. Castleton, *J. Mater. Chem. A*, 2014, **2**, 2333–2345.
16 Z. Yang, Z. Lu, G. Luo and K. Hermansson, *Phys. Lett. A*, 2007, **369**, 132–139.
17 E. L. Wilson, R. Grau-Crespo, C. L. Pang, G. Cabailh, Q. Chen, J. A. Purton, C. R. A. Catlow, W. A. Brown, N. H. de Leeuw and G. Thornton, *J. Phys. Chem. C*, 2008, **112**, 10918–10922.
18 A. D. Mayernick and M. J. Janik, *J. Chem. Phys.*, 2009, **131**, 084701.
19 T. Skála, F. Šutara, K. C. Prince and V. Matolín, *J. Phys.: Condens. Matter*, 2009, **21**, 055005.
20 J. A. Farmer, J. H. Baricuatro and C. T. Campbell, *J. Phys. Chem. C*, 2010, **114**, 17166–17172.
21 P. Luches, F. Pagliuca, S. Valeri, F. Illas, G. Preda and G. Pacchioni, *J. Phys. Chem. C*, 2012, **116**, 1122–1132.
22 Z. Yang, Z. Lu and G. Luo, *Phys. Rev. B*, 2007, **76**, 075421.
23 A. Bruix, A. Migani, G. N. Vayssilov, K. M. Neyman, J. Libuda and F. Illas, *Phys. Chem. Chem. Phys.*, 2011, **13**, 11384–11392.
24 S. Aranifard, S. C. Ammal and A. Heyden, *J. Catal.*, 2014, **309**, 314–324.
25 M. Baron, O. Bondarchuk, D. Stacchiola, S. Shaikhutdinov and H.-J. Freund, *J. Phys. Chem. C*, 2009, **113**, 6042–6049.
26 Y. Chen, P. Hu, M.-H. Lee and H. Wang, *Surf. Sci.*, 2008, **602**, 1736–1741.
27 C. Zhang, A. Michaelides, D. A. King and S. J. Jenkins, *J. Am. Chem. Soc.*, 2010, **132**, 2175–2182.
28 W.-J. Zhu, J. Zhang, X.-Q. Gong and G. Lu, *Catal. Today*, 2011, **165**, 19–24.
29 Y. Pan, N. Nilius, H.-J. Freund, J. Paier, C. Penschke and J. Sauer, *Phys. Rev. Lett.*, 2013, **111**, 206101.
30 S. J. Duclos, Y. K. Vohra, A. L. Ruoff, A. Jayaraman and G. P. Espinosa, *Phys. Rev. B*, 1988, **38**, 7755–7758.
31 J. Da Silva, M. Ganduglia-Pirovano, J. Sauer, V. Bayer and G. Kresse, *Phys. Rev. B*, 2007, **75**, 045121.
32 J. L. F. Da Silva, *Phys. Rev. B*, 2007, **76**, 193108.
33 Z. Yang, T. W. Woo, M. Baudin and K. Hermansson, *J. Chem. Phys.*, 2004, **120**, 7741–7749.
34 F. Esch, S. Fabris, L. Zhou, T. Montini, C. Africh, P. Fornasiero, G. Comelli and R. Rosei, *Science*, 2005, **309**, 752.
35 M. V. Ganduglia-Pirovano, J. L. F. Da Silva and J. Sauer, *Phys. Rev.*

Lett., 2009, **102**, 026101.
36 S. Fabris, G. Vicario, G. Balducci, S. de Gironcoli and S. Baroni, *J. Phys. Chem. B*, 2005, **109**, 22860–22867.
37 B. Cordero, V. Gómez, A. E. Platero-Prats, M. Revés, J. Echeverría, E. Cremades, F. Barragán and S. Alvarez, *Dalton Trans.*, 2008, 2832–2838.
38 H. X. Mai, L. D. Sun, Y. W. Zhang, R. Si, W. Feng, H. P. Zhang, H. C. Liu and C. H. Yan, *J. Phys. Chem. B*, 2005, **109**, 24380–24385.
39 E. Mamontov, T. Egami, R. Brezny, M. Koranne and S. Tyagi, *J. Phys. Chem. B*, 2000, **104**, 11110–11116.
40 X. Liu, K. Zhou, L. Wang, B. Wang and Y. Li, *J. Am. Chem. Soc.*, 2009, **131**, 3140–3141.
41 D. Kong, G. Wang, Y. Pan, S. Hu, J. Hou, H. Pan, C. T. Campbell and J. Zhu, *J. Phys. Chem. C*, 2011, **111**, 6715–6725.
42 C. Zhang, A. Michaelides, D. A. King and S. J. Jenkins, *Phys. Rev. B*, 2009, **79**, 075433.
43 N. V. Skorodumova, M. Baudin and K. Hermansson, *Phys. Rev. B*, 2004, **69**, 075401.
44 N. V. Skorodumova, S. I. Simak, B. I. Lundqvist, I. A. Abrikosov and B. Johansson, *Phys. Rev. Lett.*, 2002, **89**, 166601.
45 O. Hellman, N. V. Skorodumova and S. I. Simak, *Phys. Rev. Lett.*, 2012, **108**, 135504.
46 L. Pauling, *The Nature of the Chemical Bond*, Cornell University Press, Ithaca, 1960.
47 C. Zhang, A. Michaelides, D. A. King and S. J. Jenkins, *J. Chem. Phys.*, 2008, **129**, 194708.
48 A. Bruix, K. M. Neyman and F. Illas, *J. Phys. Chem. C*, 2010, **114**, 14202–14207.
49 L. Szabová, M. F. Camellone, M. Huang, V. Matolín and S. Fabris, *J. Chem. Phys.*, 2010, **133**, 234705.
50 N. C. Hernandez, R. Grau-Crespo, N. N. de Leeuw and J. F. Sanz, *Phys. Chem. Chem. Phys.*, 2009, **11**, 5246–5252.
51 H. Y. Kim, H. M. Lee and G. Henkelman, *J. Am. Chem. Soc.*, 2012, **134**, 1560–1570.
52 M. Schishkin and T. Ziegler, *Phys. Chem. Chem. Phys.*, 2014, **16**, 1798–1808.
53 M. J. Piotrowski, P. Piquini and J. L. F. Da Silva, *Phys. Rev. B*, 2010, **81**, 155446.
54 M. J. Piotrowski, P. Piquini, L. Cândido and J. L. F. Da Silva, *Phys. Chem. Chem. Phys.*, 2011, **13**, 17242–17248.
55 P. Hohenberg and W. Kohn, *Phys. Rev.*, 1964, **136**, B864–B871.
56 W. Kohn and L. J. Sham, *Phys. Rev.*, 1965, **140**, A1133–A1138.
57 J. P. Perdew, K. Burke and M. Ernzerhof, *Phys. Rev. Lett.*, 1996, **77**, 3865–3868.
58 G. Kresse and J. Hafner, *Phys. Rev. B*, 1993, **48**, 13115–13126.
59 G. Kresse and J. Furthmüller, *Phys. Rev. B*, 1996, **54**, 11169–11186.
60 S. Fabris, S. de Gironcoli, S. Baroni, G. Vicario and G. Balducci, *Phys. Rev. B*, 2005, **72**, 237102.
61 J. L. F. Da Silva, M. V. Ganduglia-Pirovano and J. Sauer, *Phys. Rev. B*, 2007, **76**, 125117.
62 S. L. Dudarev, G. A. Botton, S. Y. Savrasov, C. J. Humphreys and A. P. Sutton, *Phys. Rev. B*, 1998, **57**, 1505–1509.
63 G. Kresse, P. Blaha, J. L. F. Da Silva and M. V. Ganduglia-Pirovano, *Phys. Rev. B*, 2005, **72**, 237101.
64 J. Heyd, G. E. Scuseria and M. Ernzerhof, *J. Chem. Phys.*, 2003, **118**, 8207–8215.
65 M. J. Piotrowski, P. Piquini, M. M. Odashima and J. L. F. Da Silva, *J. Chem. Phys.*, 2011, **134**, 134105.
66 P. E. Blöchl, *Phys. Rev. B*, 1994, **50**, 17953–17979.
67 G. Kresse and D. Joubert, *Phys. Rev. B*, 1999, **59**, 1758–1775.
68 J. L. F. Da Silva, C. Stampfl and M. Scheffler, *Surf. Sci.*, 2006, **600**, 703–715.
69 W. Tang, E. Sanville, and G. Henkelman, *J. Phys.: Condens. Matter*, 2009, **21**, 084204.
70 F. Baletto and R. Ferrando, *Rev. Mod. Phys.*, 2005, **77**, 371–423.
71 J. L. F. Da Silva, M. J. Piotrowski and F. Aguilera-Granja, *Phys. Rev. B*, 2012, **86**, 125430.
72 R. Hoppe, *Angew. Chem. Int. Ed.*, 1970, **9**, 25–34.
73 R. Hoppe, *Z. Kristallogr.*, 1979, **150**, 23–52.
74 J. L. F. Da Silva, *J. Appl. Phys.*, 2011, **109**, 023502.
75 M. Nolan, S. Grigoleit, D. C. Sayle, S. C. Parker and G. W. Watson, *Surf. Sci.*, 2005, **576**, 217–229.
76 C. Zhang, A. Michaelides and S. J. Jenkins, *Phys. Chem. Chem. Phys.*, 2011, **13**, 22–33.
77 R. F. W. Bader, *Atoms in Molecules: A Quantum Theory*, Oxford University Press, Oxford, 1990.
78 G. Henkelman, A. Arnaldsson and H. Jónsson, *Comput. Mater. Sci.*, 2006, **36**, 354–360.
79 B. Hammer and J. K. Nørskov, *Surf. Sci.*, 1995, **343**, 211–220.
80 J. K. Nørskov, F. Abild-Pedersen, F. Studt and T. Bligaard, *Proc. Natl. Acad. Sci. USA*, 2011, **108**, 937–943.
81 P. Tereshchuk and J. L. F. Da Silva, *J. Phys. Chem. C*, 2012, **116**, 24695–24705.
82 P. Tereshchuk and J. L. F. Da Silva, *J. Phys. Chem. C*, 2013, **117**, 16942–16952.
83 R. L. H. Freire, A. Kiejna and J. L. F. Da Silva, *J. Phys. Chem. C*, 2014, **118**, 19051–19061.